This is a repository copy of *Composition, volume, and aspect ratio dependence of the strain distribution, band lineups and electron effective masses in self-assembled pyramidal In1-xGaxAs/GaAs and SixGe1-x/Si quantum dots* .

White Rose Research Online URL for this paper:
http://eprints.whiterose.ac.uk/1683/

Article:

Composition, volume, and aspect ratio dependence of the strain distribution, band lineups and electron effective masses in self-assembled pyramidal In$_{1-x}$Ga$_x$As/GaAs and Si$_x$Ge$_{1-x}$/Si quantum dots

M. Califano[a)] and P. Harrison
Institute of Microwaves and Photonics, School of Electronic and Electrical Engineering,
University of Leeds, LS2 9JT-Leeds, United Kingdom

We present a systematic investigation of the strain distribution of self-assembled pyramidal In$_{1-x}$Ga$_x$As/GaAs and Si$_x$Ge$_{1-x}$/Si quantum dots for the case of growth on a (001) substrate. The dependence of the biaxial and hydrostatic components of the strain on the quantum dot volume, aspect ratio, composition, and percentage of alloying x is studied using a method based on a Green's function technique. The dependence of the carriers' confining potentials and the electronic effective mass on the same parameters is then calculated in the framework of eight-band $\mathbf{k} \cdot \mathbf{p}$ theory. The results for which comparable published data are available are in good agreement with the theoretical values for strain profiles, confining potentials, and electronic effective mass. © *2002 American Institute of Physics.* [DOI: 10.1063/1.1410318]

I. INTRODUCTION

High strain epitaxy has now become a standard technique for the production of quasi-zero-dimensional systems via Stranski–Krastanov growth.[1] Due to the lattice mismatch between deposited material and substrate, the system is under high strain, which is partly relaxed by the elastic deformation leading to the formation of three-dimensional (3D) islands. The strain is therefore a key feature of the dots and causes large changes in both the band profiles and the carrier effective masses, if compared with the bulk values, which become functions of position inside the dot. Islands of various sizes and shapes have been reported,[2–6] depending on the epitaxial method and on the particular growth conditions, such as temperature, growth rate, etc. But besides the size and shape, another crucial parameter varies with the growth conditions: their composition. In fact it is now believed that even though it is possible, in principle, to achieve the formation of, say, pure InAs islands on a GaAs substrate by following a careful (i.e., low temperature, low growth rate) growth procedure, the capping process, besides altering the dot shape,[5–7] decreases the InAs composition in the islands to 60%–70%.[8] The problem is that the InAs percentage in the dot may not be constant, either, but may decrease from the top to the base of the pyramid.[8,9] A way to overcome this uncertainty about the composition could be to grow In$_{1-x}$Ga$_x$As with $x=0.5$ directly from the start, which, under certain conditions, should give dots with virtually the same composition,[10] avoiding any problems in the determination of the InAs content. The alloy island, due to the value of its lattice constant (intermediate between that of pure dot material and that of pure substrate) is expected to exhibit a different strain configuration compared to the pure dot material.

In this article we will investigate the influence of volume, aspect ratio ($Q=b/2h$, where b is the pyramid base and

h its height) and composition (percentage of alloying x) on the hydrostatic and biaxial strain components and on the related carrier confining potentials and the electronic effective mass in self-assembled pyramidal In$_{1-x}$Ga$_x$As/GaAs and Si$_x$Ge$_{1-x}$/Si quantum dots (QDs), for the case of growth on a (001) substrate. The article is organized as follows. In the next section we describe the model used for the calculations. In Sec. III we present and discuss our results and compare them with previous available theoretical calculations. Sec. IV contains the conclusions.

II. MODEL

A. Strain distribution

The strain distribution is calculated by means of the Green's function technique,[11] and takes into account the anisotropy of the elastic properties in cubic crystals. The Fourier transform of the strain tensor for QDs with cubic symmetry is[11]

$$\tilde{\varepsilon}_{ij}(\xi) = \varepsilon_0 \tilde{\chi}_{\mathrm{QD}}(\xi)$$

$$\times \left\{ \delta_{ij} - \frac{(C_{11}+2C_{12})\xi_i\xi_j/\xi^2}{1+(C_{12}+C_{44})\sum_{p=1}^{3}\dfrac{\xi_p^2}{C_{44}\xi^2+C_{\mathrm{an}}\xi_p^2}} \right. $$

$$\left. \times \frac{1}{2}\left[\frac{\xi^2}{C_{44}\xi^2+C_{\mathrm{an}}\xi_i^2} + \frac{\xi^2}{C_{44}\xi^2+C_{\mathrm{an}}\xi_j^2} \right] \right\}, \quad (1)$$

where C_{11}, C_{12}, C_{44} are the elastic moduli and $C_{\mathrm{an}}=C_{11}-C_{12}-2C_{44}$ (we use the elastic constants of the matrix for both dot and matrix material, as suggested by Andreev *et al.*[11] on the basis, among other considerations, of Keyes' scaling relationship[12])

[a)]Electronic mail: eenmc@electeng.leeds.ac.uk

389

$$\varepsilon_0 = \frac{a_S - a_{QD}}{a_{QD}}, \tag{2}$$

where a_S and a_{QD} are the lattice constants of the substrate and the QD materials, respectively; $\tilde{\chi}_{QD}(\xi)$ is the Fourier transform of the dot characteristic function (equal to 1 inside the dot and 0 outside)

$$\tilde{\chi}_{QD}(\xi) = -\frac{e^{-ih\xi_3}}{\xi_1\xi_2}\left\{ E\left(h,\xi_3 - \frac{Lx}{2h}\xi_1 - \frac{Ly}{2h}\xi_2\right) \right.$$
$$- E\left(h,\xi_3 - \frac{Lx}{2h}\xi_1 + \frac{Ly}{2h}\xi_2\right)$$
$$- E\left(h,\xi_3 + \frac{Lx}{2h}\xi_1 - \frac{Ly}{2h}\xi_2\right)$$
$$\left. + E\left(h,\xi_3 + \frac{Lx}{2h}\xi_1 + \frac{Ly}{2h}\xi_2\right) \right\} \tag{3}$$

and

$$E(a,x) = (e^{iax} - 1)/ix. \tag{4}$$

We point out that the expression we use for the Fourier transform of the dot characteristic function [Eq. (3)] is different from that reported in Ref. 11. That may partially account for the better agreement we obtain for the biaxial component with microscopic atomistic calculations of the strain distribution, such as those reported by Cusack, Briddon, and Jaros.[13] and Jiang and Singh,[14] that used the valence force field model by Keating[16] and Martin.[17]

It is interesting to mention that expression (1) is obtained by adopting for the strain the initial condition

$$\varepsilon_{ij} = \varepsilon_0 \delta_{ij}, \tag{5}$$

which implies a compressive strain along both the in-plane and growth directions, unlike the case of pseudomorphic growth of strained layers where to a compressive (tensile) in-plane strain corresponds a tensile (compressive) strain along the growth direction. If we try to force the same initial condition for a pyramidal system, the strain component along the growth direction is always positive (tensile) even at the tip of the dot, in contrast with all the previously published theoretical results.

B. Band lineups

Starting from the hydrostatic and biaxial components of the strain, we calculated the band-edge energies at the Brillouin zone center ($\mathbf{k}=0$). In the framework of the eight-band $\mathbf{k}\cdot\mathbf{p}$ theory the energy shifts are given by

$$\Delta E_c = \Delta E_c^{hy}, \tag{6}$$

$$\Delta E_{hh} = \Delta E_{v,av}^{hy} + \Delta E_{hh}^{sh}, \tag{7}$$

$$\Delta E_{lh} = \Delta E_{v,av}^{hy} + \Delta E_{lh}^{sh}, \tag{8}$$

$$\Delta E_{so} = \Delta E_{v,av}^{hy} + \Delta E_{so}^{sh}, \tag{9}$$

where

$$\Delta E_c^{hy} = a_c(\varepsilon_{xx} + \varepsilon_{yy} + \varepsilon_{zz}), \tag{10}$$
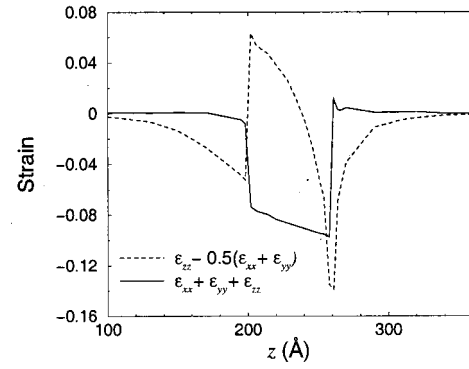

FIG. 1. Hydrostatic (full line) and biaxial (dotted line) strain components as a function of position along the height of an InAs pyramid with aspect ratio $Q=1$ ($h=60$ Å).

$$\Delta E_{v,av}^{hy} = a_v(\varepsilon_{xx} + \varepsilon_{yy} + \varepsilon_{zz}), \tag{11}$$

$$\Delta E_{hh}^{sh} = -\frac{1}{2}\delta E^{sh}, \tag{12}$$

$$\Delta E_{lh}^{sh} = -\frac{1}{2}\Delta_0 + \frac{1}{4}\delta E^{sh} + \frac{1}{2}\left[\Delta_0^2 + \Delta_0\delta E^{sh} + \frac{9}{4}(\delta E^{sh})^2\right]^{1/2}, \tag{13}$$

$$\Delta E_{so}^{sh} = -\frac{1}{2}\Delta_0 + \frac{1}{4}\delta E^{sh} - \frac{1}{2}\left[\Delta_0^2 + \Delta_0\delta E^{sh} + \frac{9}{4}(\delta E^{sh})^2\right]^{1/2}, \tag{14}$$

where Δ_0 is the spin-orbit splitting in the absence of strain.

The strain-dependent shift δE^{sh} depends on the interface orientation. In the case of growth on a (001) substrate

$$\delta E^{sh} = b(2\varepsilon_{zz} - \varepsilon_{xx} - \varepsilon_{yy}), \tag{15}$$

where b is the shear deformation potential. The hydrostatic strain component (see Fig. 1)

$$\varepsilon_h = \varepsilon_{xx} + \varepsilon_{yy} + \varepsilon_{zz} \tag{16}$$

leads therefore to a shift of both the average valence-band energy $E_{v,av}$ and the conduction-band energy E_c (a_v and a_c are the respective hydrostatic deformation potentials), whereas the direction and magnitude of the splitting of the light-, heavy-hole and split-off bands depend only on the biaxial strain (see Figs. 1 and 2)
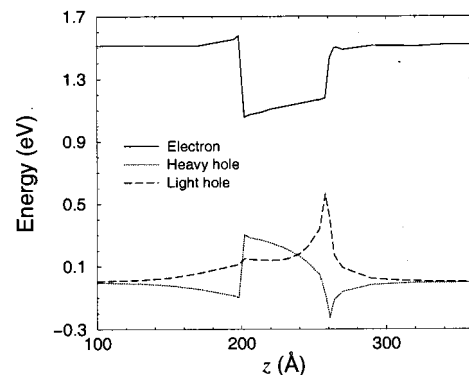

FIG. 2. Electron (full line), heavy-hole (dotted line) and light-hole (dot-dashed line) band edges as a function of position along the height of an InAs pyramid with aspect ratio $Q=1$ ($h=60$ Å).

TABLE I. Material parameters. Lattice constant a (in Å); elastic constants C_{11}, C_{12} and C_{44} (in units of 10^{12} dyne cm^{-2}; Ref. 19); Average valence-band energy $E_{v,av}$ and hydrostatic deformation potentials a_v and a_c (in eV; Ref. 20); band gap E_g (in eV; Ref. 21), spin-orbit splitting Δ_0, and shear deformation potential b (in eV; Refs. 19 and 23).

	a	C_{11}	C_{12}	C_{44}	$E_{v,av}$	Δ_0	E_g	a_v	a_c	b
InAs	6.058	0.83	0.45	0.40	−6.67	0.38	0.42	1.00	−5.08	−1.8
GaAs	5.653	1.18	0.54	0.59	−6.92	0.34	1.519	1.16	−7.17	−1.7
Si	5.431	1.675	0.650	0.801	−7.03	0.04	1.17	2.46	4.18	−2.1
Ge	5.658	1.315	0.494	0.684	−6.35	0.30	0.74	1.24	−1.54	−2.9

$$\varepsilon_b = 2\varepsilon_{zz} - \varepsilon_{xx} - \varepsilon_{yy}. \tag{17}$$

Finally, we have

$$E_c = E_{v,av} + \frac{\Delta_0}{3} + E_g + \Delta E_c^{hv}, \tag{18}$$

$$E_{hh} = E_{v,av} + \frac{\Delta_0}{3} + \Delta E_{hh}, \tag{19}$$

$$E_{lh} = E_{v,av} + \frac{\Delta_0}{3} + \Delta E_{lh}, \tag{20}$$

$$E_{so} = E_{v,av} + \frac{\Delta_0}{3} + \Delta E_{so}. \tag{21}$$

The values of the average valence-band energy $E_{v,av}$, the band-gap energy E_g, the split-off energy Δ_0, the deformation potentials a_c, a_v, and b, the lattice constant a and the elastic moduli C_{11}, C_{12} and C_{44} are reported in Table I.

C. Conduction-band effective masses

For a nondegenerate (apart from spin) band edge with energy ϵ_0 the dispersion relation for small k is parabolic in k in the vicinity of the Γ point[24]

$$\epsilon_{n\mathbf{k}} = \epsilon_{n0} + \frac{\hbar^2}{2} \sum_{\alpha\beta} k_\alpha \frac{1}{\mu_n^{\alpha\beta}} k_\beta; \quad \alpha,\beta = x,y,z, \tag{22}$$

where

$$\frac{1}{\mu_n^{\alpha\beta}} = \frac{1}{m_0} \delta_{\alpha\beta} + \frac{2}{m_0^2} \sum_{m \neq n} \frac{\pi_{mn}^\alpha \pi_{nm}^\beta}{\epsilon_{n0} - \epsilon_{m0}} \tag{23}$$

$$\pi_{mn}^\alpha = \int_{unit\ cell} u_{n0}^* p^\alpha u_{m0} d\mathbf{r} \tag{24}$$

and the spin-orbit term proportional to $\sigma \times \nabla V$ in π has been neglected. For the conduction-band edge associated with the anti-bonding s orbitals (Γ_6 symmetry), considering only the contributions of the (quadruplet) states $m = \Gamma_8$ (heavy and light holes) and (doublet) $m = \Gamma_7$ (spin-orbit split-off band), the effective mass can be expressed as[24]

$$\frac{1}{m_{\Gamma_6}} = \frac{1}{m_0} + \frac{4P^2}{3\epsilon_0} + \frac{2P^2}{3(\epsilon_0 + \Delta_0)}, \tag{25}$$

where P is the interband matrix element

$$P = \frac{-i}{m_0} \langle S|p_x|X \rangle = \frac{-i}{m_0} \langle S|p_y|Y \rangle = \frac{-i}{m_0} \langle S|p_z|Z \rangle. \tag{26}$$

From Eq. (25) we obtain

$$P^2 = \left(1 - \frac{m_{\Gamma_6}}{m_0}\right) \frac{3\hbar^2 E_g(E_g + \Delta_0)}{2m_{\Gamma_6}(3E_g + 2\Delta_0)}. \tag{27}$$

Since in the present case $m_{\Gamma_6} \ll m_0$, the term m_{Γ_6}/m_0 has been neglected. Substituting Eq. (27) (obtained in the absence of strain) into Eq. (23) (where all the matrix elements considered in the summation are proportional to P), assuming that P does not change significantly with strain, we obtained the strain-dependent expression for the effective mass tensor m_{ii}^c (the in-plane and perpendicular components are displayed in Fig. 3)

$$\frac{1}{m_\perp^c(\mathbf{r})} = \frac{1}{m_{\Gamma_6}} \left[\frac{2E_g(E_g + \Delta_0)}{(3E_g + 2\Delta_0)(V_c(\mathbf{r}) - V_{lh}(\mathbf{r}))} \right.$$
$$\left. + \frac{E_g(E_g + \Delta_0)}{(3E_g + 2\Delta_0)(V_c(\mathbf{r}) - V_{so}(\mathbf{r}))} \right]$$
$$= \frac{1}{m_{\Gamma_6}} \frac{E_g(E_g + \Delta_0)}{(3E_g + 2\Delta_0)} \frac{[3V_c(\mathbf{r}) - V_{lh}(\mathbf{r}) - 2V_{so}(\mathbf{r})]}{[V_c(\mathbf{r}) - V_{so}(\mathbf{r})][V_c(\mathbf{r}) - V_{lh}(\mathbf{r})]} \tag{28}$$
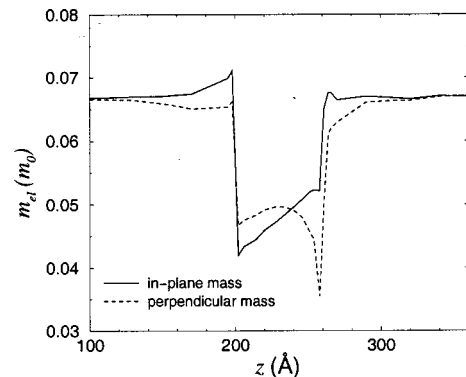
FIG. 3. In-plane (full line) and perpendicular (dotted line) electron effective mass components as a function of position along the height of an InAs pyramid with aspect ratio $Q = 1$ ($h = 60$ Å).

$$\frac{1}{m_\parallel^c(\mathbf{r})} = \frac{1}{m_{\Gamma_6}} \frac{2E_g(E_g+\Delta_0)}{(3E_g+2\Delta_0)} \left\{ \frac{0.25[V_c(\mathbf{r})-V_{hh}(\mathbf{r})][V_c(\mathbf{r})-V_{so}(\mathbf{r})]}{[V_c(\mathbf{r})-V_{hh}(\mathbf{r})][V_c(\mathbf{r})-V_{so}(\mathbf{r})][V_c(\mathbf{r})-V_{lh}(\mathbf{r})]} \right.$$

$$\left. + \frac{0.75[V_c(\mathbf{r})-V_{lh}(\mathbf{r})][V_c(\mathbf{r})-V_{so}(\mathbf{r})]}{[V_c(\mathbf{r})-V_{hh}(\mathbf{r})][V_c(\mathbf{r})-V_{so}(\mathbf{r})][V_c(\mathbf{r})-V_{lh}(\mathbf{r})]} + \frac{0.5[V_c(\mathbf{r})-V_{lh}(\mathbf{r})][V_c(\mathbf{r})-V_{hh}(\mathbf{r})]}{[V_c(\mathbf{r})-V_{hh}(\mathbf{r})][V_c(\mathbf{r})-V_{so}(\mathbf{r})][V_c(\mathbf{r})-V_{lh}(\mathbf{r})]} \right\}, \quad (29)$$

where m_{Γ_6} is the bulk electronic effective mass. A similar approach to the electron effective mass tensor was used by Fonseca et al.[25] who, nevertheless, did not take into account the coupling with the split-off band.

D. Valence-band effective masses

Unfortunately the same treatment is unsuitable for the valence-band states Γ_8 and Γ_7, because they do not couple with each other.[26] In other words, the matrix elements $\langle u_{\Gamma_{7,8}}|\mathbf{k}\cdot\mathbf{p}|u_{\Gamma_{7,8}}\rangle$ are zero for parity reasons (they are of the type $\langle n|\hat{p}^x+\hat{p}^y+\hat{p}^z|m\rangle$, where $|n\rangle,|m\rangle=|X\rangle,|Y\rangle,|Z\rangle$, and the operator $\hat{p}^\alpha$ does not connect any of those states), unless the contribution of higher (remote) valence (and/or conduction) bands is taken into account in the summation of Eq. (23). This could be regarded as a higher order contribution so that in the first approximation the heavy-hole effective masses could be considered to be independent of strain.

The problem is that according to Cusack, Briddon, and Jaros[13] the heavy-hole effective mass value in the dots is far from both the bulk and the quantum well values: their estimate for $m_{hh,z}$ (derived by performing empirical pseudopotential and ab initio local density calculations for the InAs band structure under strain, near the center of a pyramid with $h=60$ Å and $b=120$ Å), is 0.59, while the isotropic bulk value is $m_{hh}=0.40$. Strangely enough, the two-dimensional (quantum well) system value $m_{hh,z}=(\gamma_1-2\gamma_2)^{-1}=0.263$ (according to Chuang,[15] but 0.345 according to the values for γ_1 and γ_2 reported by Jiang and Singh[14]) (which is the one suggested for the dots by $\mathbf{k}\cdot\mathbf{p}$ approach) is not intermediate between the zero-and the three-dimensional system ones.

In the framework of $\mathbf{k}\cdot\mathbf{p}$ theory in order to obtain non-zero matrix elements we should use at least a 14-band Hamiltonian (which takes into account three more conduction bands), but in this case we would not know all the deformation potentials for the higher bands.

E. Alloys

The lattice constant for the ternary (T) alloy $In_{1-x}Ga_xAs$ (of the form AB_xC_{1-x}, or binary Si_xGe_{1-x},$[B_xC_{1-x}]$) was obtained from linear interpolation of that of the binary (B) constituents according to Vegard's law[21]

$$a_{ABC}(x) = xa_{AB} + (1-x)a_{AC}, \quad (30)$$

whereas for parameters such as E_g, $E_{v,av}$ and Δ_0 we used the quadratic approximation

$$T_{ABC}(x) = xB_{AB} + (1-x)B_{AC} + x(1-x)C_{ABC}, \quad (31)$$

where C is the bowing parameter, which is constant for E_g and Δ_0 ($C_{E_g}(In_{1-x}Ga_xAs)=0.38$, $C_{\Delta_0}(In_{1-x}Ga_xAs)=0.15$).[27] For Si_xGe_{1-x} the composition dependence of the valence-band spin orbit splitting is linear,[22] and since the dots are of type II, i.e., the electrons are not confined inside the dot but in the substrate, there being no need for great accuracy in the determination of the conduction-band profile, we have used a simple linear relationship for the band gap energy E_g as well). For $E_{v,av}$ the bowing parameter depends on the hydrostatic deformation potentials of the binary constituents[28]

$$C_{v,av} \simeq 3\Delta a_v \frac{\Delta a}{a_S}, \quad (32)$$

FIG. 4. Hydrostatic and biaxial strain, band edges and electron effective mass (in-plane and perpendicular) components as a function of the normalized position along the height of the pyramid, for InAs structures with aspect ratio $Q=1$ and height of 30 Å (dashed lines), 60 Å (full lines), 100 Å (dotted lines), and 150Å (dot-dashed lines).
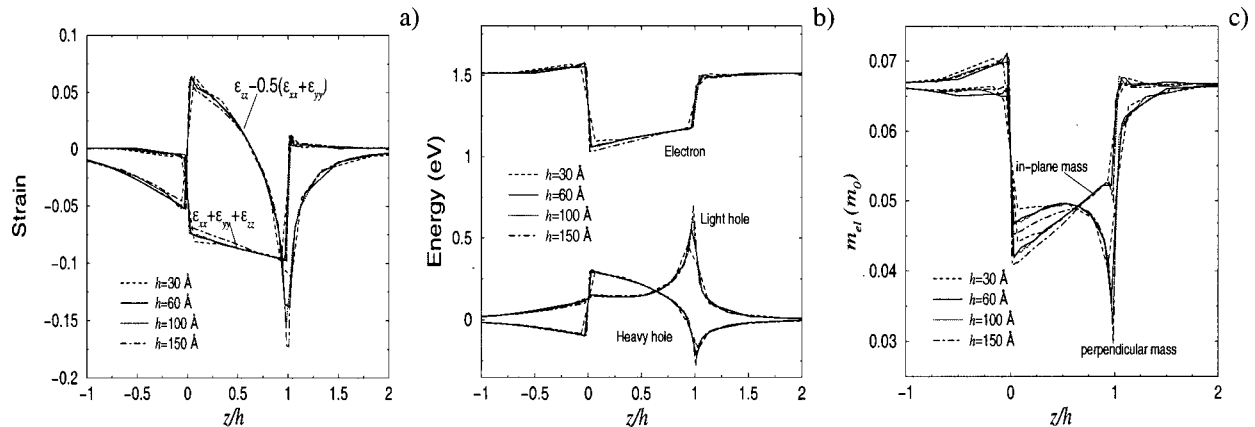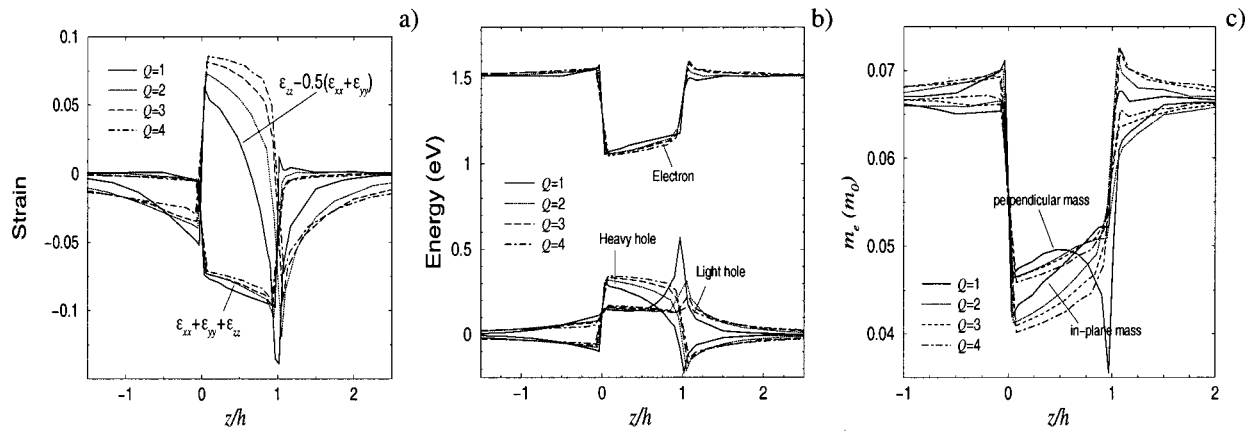
FIG. 5. Hydrostatic and biaxial strain, band edges and electron effective mass (in-plane and perpendicular) components as a function of the normalized position along the height of the pyramid, for InAs structures with aspect ratio $Q = 1$ (full lines), 2 (dotted lines), 3 (dashed lines) and 4 (dot-dashed lines).

where

$$\Delta a_v = a_v(AB) - a_v(AC) \tag{33}$$

and

$$\Delta a = a(AB) - a(AC). \tag{34}$$

III. RESULTS AND DISCUSSION

This section is divided into three subsections each of which analyzes how the dot properties we are interested in (i.e., strain distribution, band lineups and electron effective mass tensor) change by varying a different parameter. We present an investigation of their dependence on the volume, for a fixed aspect ratio $Q = 1$, in subsection III A, and on the aspect ratio (for a *virtually* constant volume) in subsection III B, for dots with pure InAs composition. Their behavior as a function of both the variables is, nevertheless, general and can be applied to other lattice mismatched, pseudomorphically grown heterostructures. Therefore, since the great majority of experimental Si/Ge QDs have Q of about $4-7$[29–32] (values for which both strain and band edge profiles are rather constant inside the dot, as can be seen below), we did not repeat the calculations for this material. We preferred, instead, to present strain and band edges for experimental samples, and compare them for different Si contents in the

last subsection, where we study the effect of varying the dot composition accounting for 30% and 50% ($x = 0.3$ to 0.5) substrate alloying. Three experimental InAs structures with aspect ratios ranging from 1.4 to 4.5 (which explains our choice of the range of variation for Q) have been considered as well.

A. Volume dependence

In Fig. 4(a) we show the variation with volume of the hydrostatic and biaxial component of the strain (as in Refs. 13 and 14, we plot $\varepsilon_{zz} - 0.5(\varepsilon_{xx} + \varepsilon_{yy}) = \varepsilon_b/2$ instead of the full biaxial strain ϵ_b) for InAs structures with aspect ratio $Q = 1$, as a function of the normalized position along the height of the pyramid. As the volume varies from 36 000 Å³ to 4 500 000 Å³, the overall shape of the curves does not change, whereas the values of both components depend weakly on the volume. This dependence is more pronounced near the base and the tip of the pyramid and reflects itself in a similar difference in the band lineups [Fig. 4(b)] and electron effective mass components [Fig. 4(c)].

The curves we obtain for both electron confining potential and effective masses of the structure with $h = 100$ Å and $b = 200$ Å are in agreement with those reported by Fonseca et al.[25] (the agreement is excellent for the electron band
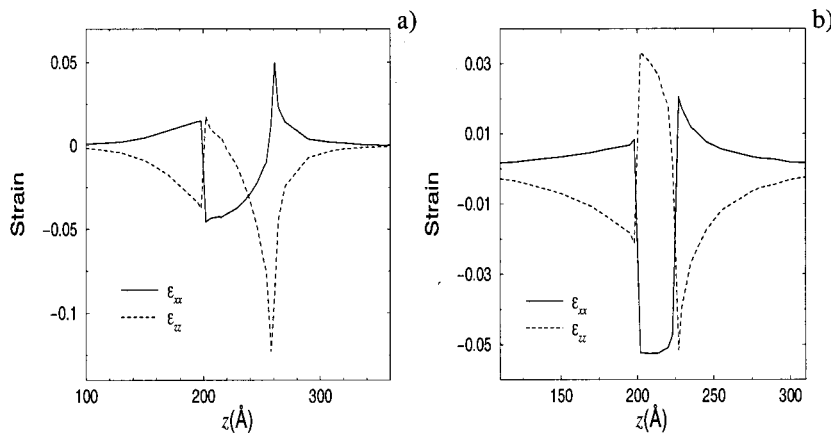

FIG. 6. In-plane (ϵ_{xx}, solid lines) and perpendicular (ϵ_{zz}, dashed lines) strain components, as a function of the position along the height of the pyramid, for InAs structures with aspect ratio $Q = 1$ and $h = 60$ Å (a), and $Q = 4$ and $h = 25$ Å (b).

TABLE II. Electronic in-plane and perpendicular effective masses (in units of m_0) and carrier confining potentials (in meV) calculated in the center of the pyramid ($h/2$) for InAs structures with aspect ratio Q ranging from 1 (four structures with different volumes) to 4.

Q	$m_{e,\perp}(h/2)$	$m_{e,\parallel}(h/2)$	$E_c(h/2)$	$E_{hh}(h/2)$	$E_{lh}(h/2)$	h	b
1	0.049	0.047	393	216	146	30	60
1	0.049	0.047	393	216	144	60	120
1	0.049	0.047	394	213	147	100	200
1	0.048	0.046	410	214	152	150	300
2	0.048	0.044	422	279	140	40	160
3	0.048	0.043	428	311	150	30	180
4	0.047	0.042	442	329	159	25	200

TABLE III. Average values of the electronic in-plane and perpendicular effective masses (in units of m_0) and carrier confining potentials (in meV) for InAs structures with aspect ratio Q ranging from 1 (four structures with different volumes) to 4.

Q	$\langle m_{e,\perp}\rangle$	$\langle m_{e,\parallel}\rangle$	$\langle E_c\rangle$	$\langle E_{hh}\rangle$	$\langle E_{lh}\rangle$	h	b
1	0.0474	0.0478	391	188	211	30	60
1	0.0466	0.0480	395	176	219	60	120
1	0.0470	0.0469	404	197	200	100	200
1	0.0460	0.0458	423	200	203	150	300
2	0.0488	0.0458	408	253	157	40	160
3	0.0491	0.0457	414	294	147	30	180
4	0.0485	0.0434	427	314	152	25	200

edge, for which we obtain the same value at the center of the pyramid. Note that in Ref. 25 on the x axis the distance is measured from the top, whereas in the present article we measure it from the bottom). Nevertheless, if we use their expressions for the effective masses (which are similar to ours but neglect the coupling with the split-off band), the results of the calculations consistently overestimate the effective masses by about 6% for all the structures considered, if compared to those obtained with our expressions (they themselves mention that the electronic energy levels obtained with their procedure are 5%–10% higher than the exact values, if compared with an eight-band **k·p** calculation. In fact, neglecting the coupling between the light-hole and the split-off bands can lead to an error in the light-hole energies comparable to the light- and heavy-hole energy splittings which could be several tens of meV and too large to be ignored.[15] This, in turn, is expected to affect the value of the electronic effective mass components). If we compare the value for the perpendicular component of the effective mass in the center of the pyramid reported in Ref. 25 (we choose this point to conform to the choice of Cusack, Briddon, and Jaros[13,18]) with the value in the same point from Fig. 4, the overestimate is about 4%.

The average value of the effective mass of all three structures, which is a factor of 2 larger than the bulk value (see Table II), is in agreement with that calculated by Cusack, Briddon, and Jaros.[13]

B. Dependence on Q

The situation is completely different when we keep the volume *virtually* constant and vary the aspect ratio Q between 1 and 4 (as shown below, this variation covers most of the experimental samples obtained so far by epitaxial growth). The largest variation in volume is from 288 000 to 341 333 Å^3, which correspond to a variation of the dimensions of the dot from $h=60$ Å and $b=120$ Å, to $h=63.5$ Å and $b=127$ Å, which, as can be seen in Fig. 4(a), does not introduce any detectable variation in the strain curves. Figure 5 displays the results of our calculations. For $Q=1$ the biaxial strain becomes negative at about 2/3 of the pyramid height. This means that the ε_{zz} strain tensor component equals the $\varepsilon_{xx}=\varepsilon_{yy}$ one (pure hydrostatic pressure) at that point, in excellent agreement with the results reported by Cusack and co-workers.[18] As a consequence of this change of sign of the biaxial component (see Fig. 5(b), the heavy-hole band edge becomes lower in energy than the light hole one [see Eq. (12)]. For higher Qs this transition occurs much nearer to the tip (at about 1/10 of the height from it, for $Q=2$, and at the tip, for $Q=3,4$). The strain profile for $Q=4$ is in agreement with that reported by Cusack and co-workers[18] for a structure of the same dimensions, where no region of purely compressive stress was found within the dot, and therefore the heavy-and light-hole potentials were well separated [as in Fig. 5(b)]. Moreover, the biaxial
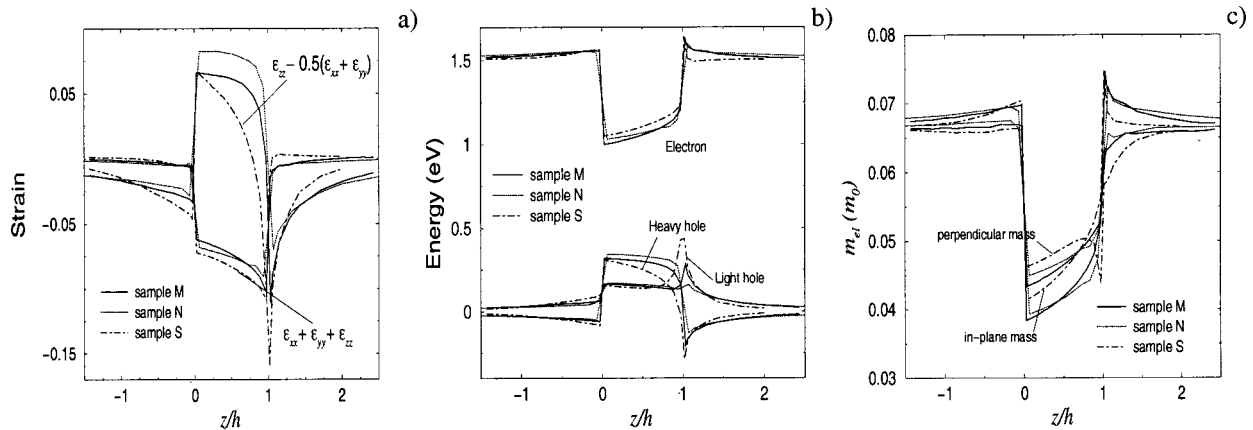

FIG. 7. Hydrostatic and biaxial strain, band edges and electron effective mass (in-plane and perpendicular) components as a function of the normalized position along the height of the pyramid, for InAs experimental structures with aspect ratio $Q=1.4$ (dotted lines), 2.8 (full lines) and 4.5 (dot-dashed lines).

TABLE IV. Electronic in-plane and perpendicular effective masses (in units of m_0) and carrier confining potentials (in meV) calculated in the center of the pyramid ($h/2$) for three experimental InAs structures with aspect ratio Q ranging from 1.4 to 4.5 (since the last pyramid has a rectangular base we report both dimensions).

Q	$m_{e,\perp}(h/2)$	$m_{e,\parallel}(h/2)$	$E_c(h/2)$	$E_{hh}(h/2)$	$E_{lh}(h/2)$	h	b
1.4[a]	0.049	0.045	414	253	135	70	200
2.8[b]	0.046	0.042	463	300	150	70	400
4.5[c]	0.047	0.041	452	332	161	30	300–250

[a]Reference 33.
[b]Reference 34.
[c]Reference 35.

TABLE V. Average values of the electronic in-plane and perpendicular effective masses (in units of m_0) and carrier confining potentials (in meV) for three experimental InAs structures with aspect ratio Q ranging from 1.4 to 4.5 (since the last pyramid has a rectangular base we report both dimensions).

Q	$\langle m_{e,\perp}\rangle$	$\langle m_{e,\parallel}\rangle$	$\langle E_c\rangle$	$\langle E_{hh}\rangle$	$\langle E_{lh}\rangle$	h	b
1.4[a]	0.048	0.046	408	228	173	70	200
2.8[b]	0.047	0.042	454	287	151	70	400
4.5[c]	0.047	0.042	442	321	156	30	300–250

[a]Reference 33.
[b]Reference 34.
[c]Reference 35.

strain maximum increases with Q, whereas its minimum decreases. Another interesting feature is that with increasing Q the depth (both absolute and measured in units of the pyramid height) of the region of substrate above the dot where the biaxial strain component is nonzero also increases. In other words, the lower the height (the flatter the pyramid) the deeper the effect of the strain on the substrate above it.

These differences in behavior for different Qs (as opposed to the almost unchanged shapes of the curves for different volumes), can be explained in terms of the different effects the surrounding (substrate and barrier) material produces on dots of different shape. For all Qs the in-plane lattice constant is compressed by the substrate near the base [which gives a negative ε_{xx} and a positive ε_{zz} component, see Figs. 6(a) and 6(b)]. For low Q structures, however, as one moves towards the tip, the barrier material that surrounds the dot compresses the perpendicular lattice constant as well, producing a region where both ε_{zz} and ε_{xx} are negative, till, nearer to the apex, the ε_{xx} component becomes positive [as in Fig. 6(a)]. High Q pyramids, instead, are flatter and the compression caused by the substrate to the sides is not enough to produce any change in sign of the strain tensor components. This means that ε_{zz} at the pyramid tip is still positive [i.e., the dot perpendicular lattice constant is still larger than the unstrained one, as in Fig. 6(b)], and therefore no region of pure hydrostatic pressure is found within

the dot. As a consequence, no crossing between the heavy- and light-hole bands occurs within the dot and the region of the substrate above it where the barrier material ε_{zz} stays negative (i.e., where the barrier material z lattice constant is smaller than the unstrained one) increases (in other words, since the z component of the strain at the pyramid tip is still tensile, the region immediately above it must be under a compressive strain along that direction).

This is a factor that has to be taken into account when stacked arrays of self-assembled QDs are grown. High Q dots will, in fact, require thicker spacing layers to be considered isolated (electronically decoupled), than needed by low Q dots. On the other hand, if one wants to achieve vertical alignment and coupling of QDs by exploiting the strain coupling effect, the growth of high or low Q dots allows the spacing layer to be tailored to suit any particular device requirement.

Even though Fig. 5 seems to suggest a similar increase also in the region below the pyramid, this effect is only due to the normalization. If plotted on an absolute scale, there is no difference in the extension of this region for the different values of Q considered here.

Both the hydrostatic and the biaxial components are in good agreement almost everywhere with microscopic atomistic calculations of the strain distribution such as those reported (for a structure with $h = 60$ Å and $b = 120$ Å) by Cusack, Briddon, and Jaros,[13] and Jiang and Singh,[14] that used
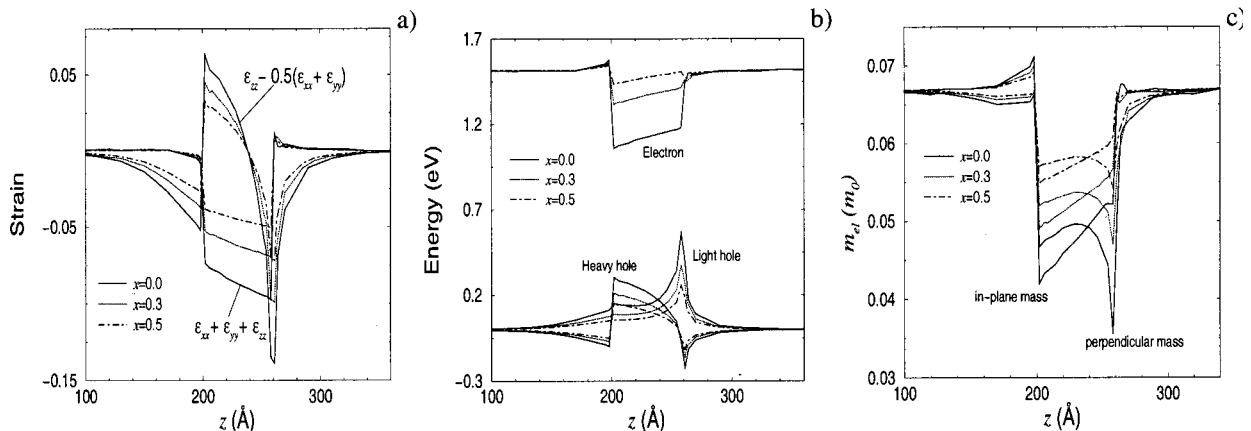

FIG. 8. Hydrostatic and biaxial strain, band edges and electron effective mass (in-plane and perpendicular) components as a function of the position along the height of the pyramid, for In$_{1-x}$Ga$_x$As structures with aspect ratio $Q=1$ ($h=60$ Å) and GaAs composition $x=0$ (full lines), 0.3 (dotted lines) and 0.5 (dot-dashed lines).

TABLE VI. Electronic in-plane and perpendicular effective masses (in units of m_0) and carrier confining potentials (in meV) calculated in the center of the pyramid ($h/2$) for $In_{1-x}Ga_xAs$ structures with aspect ratio $Q=1$ and GaAs composition $x=0$, 0.3 and 0.5.

x	$m_{e,\perp}(h/2)$	$m_{e,\parallel}(h/2)$	$E_c(h/2)$	$E_{hh}(h/2)$	$E_{lh}(h/2)$	h	b
0.0	0.049	0.047	393	216	144	60	120
0.3	0.053	0.052	146	150	99	60	120
0.5	0.058	0.057	42	106	69	60	120

TABLE VII. Average values of the electronic in-plane and perpendicular effective masses (in units of m_0) and carrier confining potentials (in meV) for $In_{1-x}Ga_xAs$ structures with aspect ratio $Q=1$ and GaAs composition $x=0$, 0.3 and 0.5.

x	$\langle m_{e,\perp}\rangle$	$\langle m_{e,\parallel}\rangle$	$\langle E_c\rangle$	$\langle E_{hh}\rangle$	$\langle E_{lh}\rangle$	h	b
0.0	0.046	0.048	395	176	219	60	120
0.3	0.052	0.052	148	123	142	60	120
0.5	0.057	0.057	44	87	97	60	120

the valence force field model by Keating[16] and Martin.[17] The maximum value for the biaxial strain we calculate at the base of the pyramid is, nevertheless, about 30% lower than that reported in the cited works (see Fig. 1). This is expected to affect the biaxial-strain-dependent shift δE^{sh} between the valence bands at that point. Comparison with the hole potential profiles reported by Cusack and co-workers in Ref. 18 shows that the light-hole band edge at the base of the dot for the structure with $Q=1$ in Fig. 2 has actually a value about 20% lower than that resulting from their calculations. The same comparison for the structure with $Q=4$ reveals that, even though the overall shape of the band edge profiles shown in Fig. 5 is in agreement with that reported in Ref. 18, our calculated values are underestimated.

If, on the other hand, we compare our results (Fig. 4, dashed lines) with the strain profiles reported by Andreev et al.[11] for a pyramid with $b=60$ Å and $h=30$ Å, we find that both the strain components are in very good agreement almost everywhere except at the tip of the dot where the biaxial strain value they calculated is about 70% higher than that shown in Fig. 4, whereas the agreement is still good for the hydrostatic component. This discrepancy is hard to explain, since we use the same expression for the Fourier transform of the strain tensor. However, the choice of other parameters such as the integration domain and the number of sampling points for the calculation of the three-dimensional inverse Fourier transform integral in the momentum space may have affected the results.

The most relevant feature about the band edges that emerges from the comparison among the curves in Fig. 5 is that with increasing Q the overall depth of both the electron and hole confining potentials increases and becomes less variable with position (i.e., more potential-well-like) inside the dot. All this has the effect of decreasing the value of both the electronic effective mass components $m_{e,\perp}$ and $m_{e,\parallel}$ with increasing Q.

In Tables II and III we present the results of our calculations for the electronic in-plane and perpendicular effective masses (in units of m_0) and carrier confining potentials (in meV) (both on average and calculated in the center of the pyramid $h/2$) for InAs structures with aspect ratio Q ranging from 1 (four structures with different volumes) to 4.

The value of the perpendicular (i.e., along the growth direction) electron effective mass calculated in the center of the pyramid decreases by about 2% with increasing volume for a fixed Q (and up to twice as much with increasing Q), in passing from the first structure to the fourth, whereas the in-plane component has a similar behavior with increasing volume but a greater decrease (about 10%) with increasing Q, if we compare the same two structures. The electron confining potential in the dot center increases by more than 12% with Q increasing from 1 to 4, and by about 4% increasing the volume from 36 000 to 4 500 000 Å^3 for $Q=1$. The heavy-hole band edge position in the center of the pyramid slightly decreases with increasing volume, whereas it increases by more than 50% when Q passes from 1 to 4. A similar behavior is found for the average values of these quantities.

In Fig. 7 we compare the strain, band edges and effective masses profiles for three experimental InAs QDs grown by Schmidt et al.,[33] Murray et al.[34] and Noda, Abe, and Tamura,[35] respectively, with aspect ratios ranging from about 1.4 to about 4.5. The relevant quantities are reported in Tables IV and V.
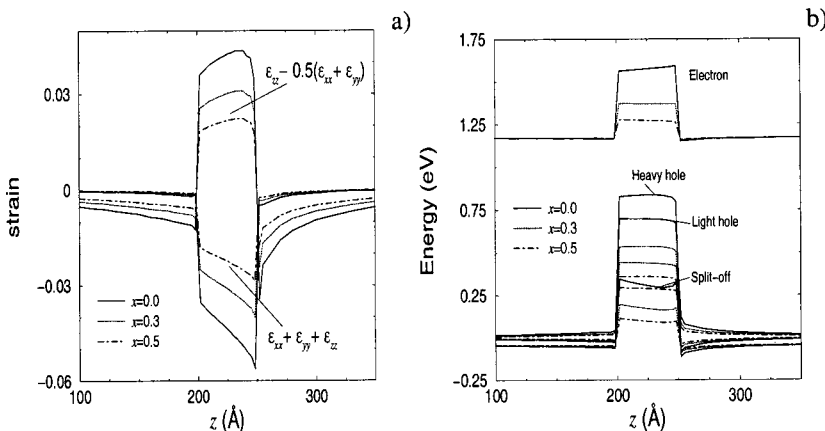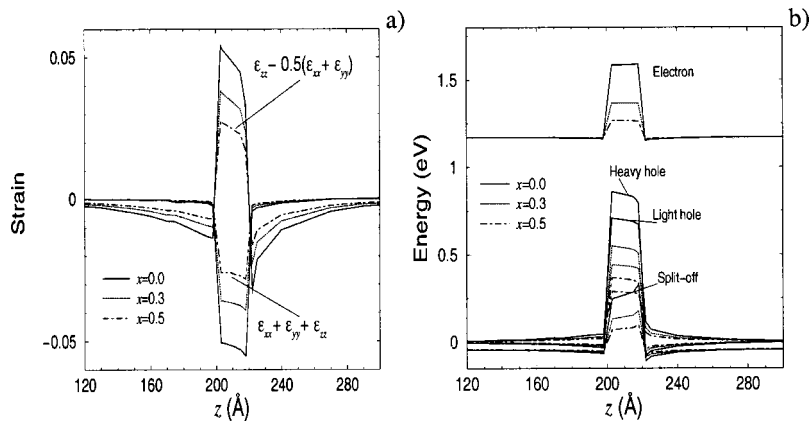

FIG. 9. Hydrostatic and biaxial strain components (a) and band edge profiles (b) as a function of the position along the height of the pyramid, for experimental Si_xGe_{1-x}/Si structures (see Ref. 30) with aspect ratio $Q=6$ and Si composition $x=0$ (full lines), 0.3 (dotted lines) and 0.5 (dot-dashed lines).

FIG. 10. Hydrostatic and biaxial strain components (a) and band edge profiles (b) as a function of the position along the height of the pyramid, for experimental Si_xGe_{1-x}/Si structures (see Ref. 29) with aspect ratio $Q=5$ and Si composition $x=0$ (full lines), 0.3 (dotted lines) and 0.5 (dot-dashed lines).

C. Alloying

When alloying (or intermixing) occurs during (or after) the growth process, the lattice mismatch between substrate and dot material is reduced, with a consequent proportional (we only consider alloys with uniform composition) reduction of the strain induced by it. This is shown in Fig. 8, where we compare biaxial and hydrostatic strain for $In_{1-x}Ga_xAs$ pyramids with $Q=1$ ($h=60$ Å) and a GaAs composition $x=0$, 0.3 and 0.5.

If we consider the energy lineups, it is apparent that with increasing GaAs composition both electrons and holes become progressively more weakly bound, due to the reduced difference in the carrier band edge positions between substrate and alloy dot. The electron confining potential undergoes the largest variation, decreasing from an average value of about 400 meV for $x=0$ to a value of only a few tens of meV (about 40 meV) for $x=0.5$, which, according to our calculations is not enough to trap any electron inside the dot (we assume a constant 3D confining potential inside the pyramid. See Ref. 36 for more details about the method employed). Even though its value at the base of the pyramid is of about 90 meV and stays higher than 50 meV almost until one half of the height, the potential well is still not sufficiently deep to bound an electron. The fact that $In_{1-x}Ga_xAs$ dots with a nominal In content of $x=0.5$ do actually have bound electronic levels may be explained in the light of recent experiments[37] which have found a highly nonuniform composition with an In-rich core having an inverted-pyramid (or-cone) shape in such structures. This In-rich region would then be responsible for trapping the electrons.

The electron effective masses (calculated in the center of the pyramid) follow a quasilinear behavior in passing from the value of 0.049 (for the perpendicular and 0.047 for the in-plane component respectively), for $x=0$ to 0.058(0.057) for $x=0.5$ (the same is true for their average value, as shown in Tables VI and VII, where we present our results for the carrier confining potentials as well).

The same trend has been found for the $Si_xGe_{(1-x)}/Si$ experimental structures considered, as shown in Figs. 9 and 10, where we compare, for two different experimental samples,[29,30] the strain and band edge profiles for x varying between 0 and 0.5.

IV. CONCLUSIONS

We have presented an investigation of the strain distribution of self-assembled pyramidal $In_{1-x}Ga_xAs/GaAs$ and Si_xGe_{1-x}/Si quantum dots in the case of growth on a (001) substrate, where the dependence of the biaxial and hydrostatic components on the quantum dot volume, aspect ratio, composition and percentage of alloying x has been calculated using a method based on the Green's function technique.

The dependence of the carriers' confining potentials on the same parameters has then been calculated in the framework of eight-band $\mathbf{k} \cdot \mathbf{p}$ theory. In this framework we derived an expression for the electron effective mass in-plane and perpendicular components which takes into account the coupling with the spin-orbit split-off band and demonstrated the importance of this inclusion by comparing our results with other published data, where this coupling is neglected.

Good agreement is obtained from the comparison (where possible) with theoretical values for strain profiles, confining potentials and electronic effective mass reported in the literature.

ACKNOWLEDGMENTS

[1] I. N. Stranski and L. Von Krastanov, Akad. Wiss. Lit. Mainz Math.-Natur. Kl. IIb **146**, 797 (1939).
[2] M. Grundmann, J. Christen, N. N. Ledentsov, J. Böhrer, D. Bimberg, S. S. Ruvimov, P. Werner, U. Richter, U. Gösele, J. Heydenreich, V. M. Ustinov, A. Yu. Egorov, A. E. Zhukov, P. S. Kop'ev, and Zh. I. Alferov, Phys. Rev. Lett. **74**, 4043 (1995).
[3] D. Leonard, K. Pond, and P. M. Petroff, Phys. Rev. B **50**, 11 687 (1994).
[4] J. M. Moison, F. Houzay, F. Barthe, L. Leprince, E. Andre and O. Vatel, Appl. Phys. Lett. **64**, 196 (1994).
[5] M. Fricke, A. Lorke, J. P. Kotthaus, G. Medeiros-Ribeiro, and P. M. Petroff, Europhys. Lett. **36**, 197 (1996).
[6] S. Sauvage, P. Boucaud, F. H. Julien, J.-M. Gerard, and J.-Y. Marzin, J. Appl. Phys. **82**, 3396 (1997).

[7] Y. Nabetani, T. Ishikawa, S. Noda, and A. Sakai, J. Appl. Phys. **76**, 347 (1994).

[8] D. Zhi, H. Davoc, R. Murray, C. Roberts, T. S. Jones, D. W. Pashley, P. J. Goodhew, and B. A. Joyce, J. Appl. Phys. **89**, 2079 (2001).

[9] I. Kegel, T. H. Metzger, A. Lorke, J. Peisl, J. Stangl, G. Bauer, J. M. Garcia, and P. M. Petroff, Phys. Rev. Lett. **85**, 1694 (2000).

[10] M. Henini (private communication).

[11] A. D. Andreev, J. R. Downes, D. A. Faux, and E. P. O'Reilly, J. Appl. Phys. **86**, 297 (1999).

[12] R. W. Keyes, J. Appl. Phys. **33**, 3371 (1962).

[13] M. A. Cusack, P. R. Briddon, and M. Jaros, Phys. Rev. B **54**, R2300 (1996).

[14] H. Jiang and J. Singh, Phys. Rev. B **56**, 4696 (1997).

[15] P. N. Keating, Phys. Rev. **145**, 637 (1966).

[16] R. M. Martin, Phys. Rev. B **1**, 4005 (1969).

[17] Landolt-Bornstein, *Numerical Data and Functional Relationships in Science and Technology*, Group III, vol. 17a, edited by O. Madelung (Springer, New York, 1982).

[18] C. G. Van de Walle, Phys. Rev. B **39**, 1871 (1989).

[19] J. H. Davies, *The Physics of Low-Dimensional Semiconductors—An introduction* (Cambridge University Press, Cambridge, 1998).

[20] H. C. Casey and M. B. Panish, *Heterostructure Lasers, Part B: Materials and Operating Characteristics* (Academic, New York, 1978).

[21] G. Bastard, *Monographies de Physique—Wave Mechanics Applied To Semiconductor Heterostructures* (Les Editions de Physique, Les Ulis, 1992).

[22] L. R. C. Fonseca, J. L. Jimenez, J. P. Leburton, and R. M. Martin, Phys. Rev. B **57**, 4017 (1998).

[23] M. Grundmann, O. Stier, and D. Bimberg, Phys. Rev. B **52**, 11969 (1995).

[24] S. L. Chuang, *Physics of Optoelectronic Devices* (Wiley, New York, 1995).

[25] M. P. C. M. Krijn, Semicond. Sci. Technol. **6**, 27 (1991).

[26] R. Braunstein, Phys. Rev. **130**, 869 (1963).

[27] M. Cardona and N. E. Christensen, Phys. Rev. B **37**, 1011 (1988).

[28] C. Miesner, O. Röthig, K. Brunner, and G. Abstreiter, Appl. Phys. Lett. **76**, 1027 (2000); C. Miesner, K. Brunner, and G. Abstreiter (unpublished).

[29] M. Hallsal and A. Dunbar (private communication).

[30] J. L. Liu, Y. S. Tang, K. L. Wang, T. Radetic, and R. Gronsky, Appl. Phys. Lett. **74**, 1863 (1999).

[31] V. Le Thanh, V. Yam, P. Boucaud, F. Fortuna, C. Ulysse, D. Bouchier, L. Vrvoort, and J.-M. Lourtioz, Phys. Rev. B **60**, 5851 (1999).

[32] M. A. Cusack, P. R. Briddon, and M. Jaros, Phys. Rev. B **56**, 4047 (1997).

[33] K. H. Schmidt, G. Medeiros-Ribeiro, M. Oestreich, P. M. Petroff, and G. H. Dohler, Phys. Rev. B **54**, 11346 (1996).

[34] R. Murray, D. Childs, S. Malik, P. Siverns, C. Roberts, J.-M. Hartmann, and P. Stavrinou, Jpn. J. Appl. Phys., Part 1 **38**, 528 (1999).

[35] S. Noda, T. Abe, and M. Tamura, Physica E (Amsterdam) **2**, 643 (1998).

[36] M. Califano and P. Harrison, Phys. Rev. B **61**, 10959 (2000).

[37] N. Liu, J. Tersoff, O. Baklenov, A. L. Holmes, Jr., and C. K. Shih, Phys. Rev. Lett. **84**, 334 (2000).